Epipolar Rectification of a Generic Camera

Marc Pierrot-Deseilligny, Ewelina Rupnik

Univ Gustave Eiffel, Géodata Paris, IGN, LASTIG, F-77454 Marne-la-Vallée, France
(marc.pierrot-deseilligny, ewelina.rupnik)@ign.fr

Keywords: photogrammetry, epipolar geometry, generic camera, pushbroom sensor, central perspective

Abstract

We propose a generic method for epipolar resampling that is not tied to a specific camera model. We demonstrate the effectiveness of the approach on a central perspective, pushbroom and pushbroom panoramic camera models. We also devise an *epipolarability index* that measures the suitability of an image pair for epipolar rectification, and provide a formal derivation of the ambiguity bound to epipolar resampling. An open-source implementation of the algorithm is available at `github.com/micmacIGN/micmac`.

1. Introduction

The epipolar geometry of images plays a central role in numerous applications within photogrammetry and computer vision. In a stereo-reconstruction pipeline, it is involved at two key stages: camera pose orientation and dense image matching. In the camera pose orientation step, the epipolar geometry is used when determining the relative orientation of an image pair from their point correspondences. Assuming a central-perspective projection model and known internal calibration, the epipolar geometry can be estimated through the essential matrix. From this estimate, the relative orientation of the cameras is subsequently recovered (Fusiello et al., 2000). In the dense image matching step, epipolar rectification simplifies the correspondence search: for any point (x_1, y) in image I_1, its match must lie at some point (x_2, y) in image I_2. Consequently, establishing correspondences across the images is reduced to a one-dimensional (1D) search problem. In this paper, we only look at the epipolar rectification problem and more specifically its application to a generic camera model.

1.1 Related works

Central projection camera model. Rectifying a central perspective camera stereo pair involves transforming their original epipolar geometry to a canonical form where: (a) their focal planes are coplanar, and (b) their conjugate epipolar lines are colinear, and parallel to the camera's x-axis. From the algebraic standpoint, this is equivalent to applying two 2-dimensional (2D) projective transformations to both images of the stereo pair. Several approaches to computing such transformations have been proposed over the course of the last 30 years. For a calibrated stereo pair (i.e. with known camera projection matrices), there exists a unique rectifying transformation, up to a rotation along the baseline (Fusiello et al., 2000). In an uncalibrated case, the solution is obtained by factoring out two 2D homographies from the fundamental matrix. Because there are no two unique homographies, the common practice is to parametrize these transformations such that the distortions caused by the rectification process are minimized. For instance, (Loop and Zhang, 1999) decompose the rectifying homographies to a combination of the projective, similarity and shearing transforms, with the condition that the prrojective transform remains (close to) affine. (Hartley, 1999) satisfies the condition that for a neighborhood of a point (e.g. the center of an image), the computed homography is a rigid transformation. Building on this work, (Isgrò and Trucco, 1999)'s approach obtains a unique solution by minimizing the x-disparity without having to explicitly calculate the fundamental matrix. Instead of minimizing the disparity in the first coordinate, (Wu and Yu, 2005) recycle an idea first introduced by (Hartley, 1999) which requires that the aspect ratio of the images before and after rectification is constant. (Fusiello and Irsara, 2008) introduced the camera matrices back into the equation and proposed a *quasi*-Euclidean approach for uncalibrated cameras, similar to that of the calibrated cameras case. Their projective transformations are parametrized by five angles and a focal length. (Pascal Monasse, 2010) break down the one-time rotation of (Fusiello and Irsara, 2008) to a three step procedure, and prove increased robustness by using a geometric error measure (i.e., camera rotation angle) to reduce the rectifying error distortions. A different approach (Darmon and Monasse, 2021) addresses the scenario when one of the epipoles is defined in the image domain and proposes a rectification minimising large perspective distortions by relying on a polar transform. A family of recent deep learning approaches circumvents the need for epipolar rectification by implicitly modelling it within a multi-view stereo matching framework (Wang et al., 2025, Wang et al., 2024). Nevertheless, learning-based stereo and multi-view stereo methods relying on rigorous epipolar constraint modelling remain the more precise and more robust options (Lipson et al., 2021, Xu et al., 2023).

Pushbroom sensors. Unlike the central projection camera model, pushbroom-like sensors acquire each image row from a different perspective center. As a consequence, the epipolar lines are neither straight lines, nor are they conjugate across the image (Gupta and Hartley, 1997). One way to overcome this particularity is to simplify the projection function with a 2D affine (Ono, 1999, Wang et al., 2011) or a parallel projection model (Morgan et al., 2006). Such approximations usually come at the price of precision, especially with the increasing camera field-of-view or in mountainous scenes. By extending the 2D affine model with two quaratic terms, (Okamoto. et al., 1999) demonstrates improved performance on SPOT images. In the context of dense image matching, (de Franchis et al., 2014) improves the precision by partitioning the images into small patches, for which indepedent affine rectifictions are computed. Alternatively, and with equally good precision, (Oh, 2011) uses the *Rational Polynomial Coefficients* (RPCs) to map the epi-

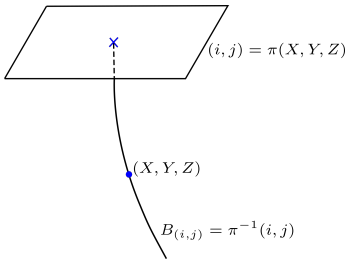

Figure 1. Generic sensor model. A projection π and a bundle B corresponding to a point (X, Y, Z).

polar curves across the full size images with lines, in a piecewise approach, followed by a global rectification transformation using a polynomial function of 3^{rd} order. More recently, (Liao et al., 2022) proposes an approach that simultaneously rectifies the images to orthoprojections and iteratively builds a surface model.

1.2 Contributions

Our research work proposes an epipolar geometry rectification method that is not tied to any camera physical model. We provide a theoretical derivation and demonstrate the effectiveness of the approach on a range of models, including Pleiades images (pushbroom), the Corona images (panoramic pushbroom) and a consumer grade camera images (central perspective). The method resembles (Oh, 2011) approach in that it exploits the point correspondences to find the polynomial mapping to epipolar geometry. However, unlike the work of (Oh, 2011), we do not require that the camera geometric model is known. We demonstrate that in some circumstances, point correspondences obtained from an image processing routine, e.g. SIFT (Lowe, 2004), can serve to find the epipolar resampling. Finally, we formally derive the ambiguity of the epipolar geometry, and propose an *epipolarability index* that quantitatively describes the existence of epipolar geometry between a pair of images.

2. Brief theoretical aspect of epipolar geometry for the generic case

Below, we give the minimal formal definitions necessary to understand the method from a practical point of view. More rigorous analysis and a full demonstration can be found in Appendix A. We have the following definition:

1. A geometric sensor establishes a relation between a 3D point and the image point, it is formalized by a mapping π from $\mathbb{R}^3$ to $\mathbb{R}^2$ (Figure 1);
2. The bundle $\mathcal{B}$ of an image point p is the $3d$ curve $\pi^{-1}(p)$;
3. Two points p_1 and p_2 in two different images are potentially homologous if their bundles intersect in some 3D point, we note it $p_1 \overset{\Longleftrightarrow}{\pi_1,\pi_2} p_2$ (Figure 2) and refer to it as H-compatible;
4. An epipolar geometry of two images is a pair ϕ_1, ϕ_2 of image mapping such that point p_1 and p_2 are potential homologous iff their resampled points have the same ordinates (Figure 3 and more formal definition in Appendix, Definition 5).

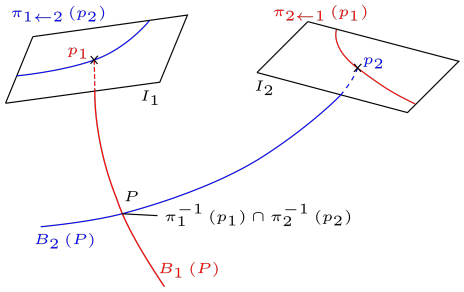

Figure 2. H-compatibility $\overset{\Longleftrightarrow}{\pi_1,\pi_2}$. See definition in Appendix.

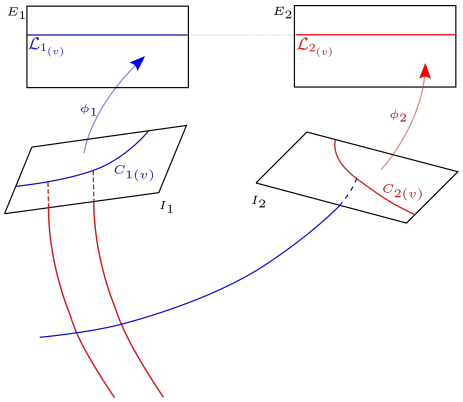

Figure 3. Epipolar geometry. $\mathcal{L}_k(v)$ and $\mathcal{C}_k(v)$ are the epipolar line and curve. See definitions in Appendix.

In mathematics, one generally prefers objects that both exist and are unique. This is not the case for epipolar geometry: for a generic pair of sensors π_1, π_2 it often does not exist, and when it does, it is not unique. For the existence of epipolar geometry, a necessary and sufficient condition is that the curves $\pi_1^{-1}(p)$ and $\pi_2^{-1}(p)$ are globally homologous, which is equivalent to $\pi_2^{-1}(\pi_2(\mathcal{B}_1)) = \mathcal{B}_1$. Interestingly, this global condition can be replaced by a local equation that quantifies a degree to which the epipolar geometry exists (see Theorem 1 in Appendix A). In practice, the non-existence of a perfect epipolar geometry is less problematic, as a quasi-epipolar geometry typically exists and the residual in Theorem 1 becomes negligible. The issue of non-uniqueness, however, requires more careful treatment to ensure a well-posed estimation problem. When an epipolar geometry does exist, it is defined only up to the following ambiguities (see Figure 4):

1. Any pair of deformations of epipolar images that is stable inside lines of the images;
2. A global transformation of the lines.

By resolving these two ambiguities, a unique epipolar geometry can be determined (see Theorem 2 in Appendix A).

3. Proposed method for epipolar geometry resampling

3.1 Hypothesis and layout

3.1.1 Principles The principle of the method is to use *H-Compatible* points p_1, p_2 to calculate a pair of mapping functions ϕ_1, ϕ_2 (i.e., resampling) that comply with the epipolar constraint, i.e. *"$\phi_1(p_1)$ and $\phi_2(p_2)$ are on the same line"*:

$$\phi_1(x, y) = (x, y') \tag{1}$$

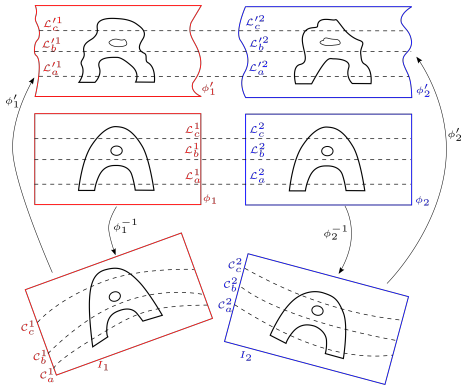

Figure 4. Ambiguity of the epipolar geometry: two possible epipolar resamplings for a single stereo pair.

$$\phi_2(x, y) = (x, y') \tag{2}$$

$$\phi_1(0, y) = (0, y) \tag{3}$$

As these epipolar functions are not unique, we parameterize the mapping ϕ_k accordingly:

$$\phi_k(i, j) = (i, V_k(i, j)); \quad V_k : \mathbb{R}^2 \to \mathbb{R} \tag{4}$$

This parametrization implements the constraints of Equations (1) and (2). We will account for the constraint of Equation (3) in Section 3.2.1. To compute V_1, V_2, for any pair of *H-Compatible* points, we add an observation that constrains V_1 and V_2:

$$V_1(p_1) = V_2(p_2). \tag{5}$$

3.1.2 Hypothesis The method takes two camera models π_1 and π_2 as inputs. These models are considered black-boxes that satisfy the ground-to-image mapping Equation (18) (Appendix A), and for which no specific assumption is made on the physical model of the camera. In our C++ implementation, the cameras are considered to be pure virtual classes offering the interface to Equation (18) (Appendix A). In this paper, the examples processed by our method are pushbroom satellite models known by their RPCs and the central perspective. However, the only restriction imposed on the generic nature of the model is that the projection function is ”smooth”, i.e.: (1) π are $\mathcal{C}^\infty$ functions, and (2) the directions of epipolar curves vary within a limited range (for example, less than $\frac{\pi}{2}$). Figure 5 illustrates the latter constraint. The left image presents a set of epipolar lines with too large direction variations. The right images represent pairs of epipolar lines whose directions change within a small range, therefore suitable for the proposed resampling method.

3.1.3 Estimation of the center and the global direction Before calculating the rectifying functions V_k, we need to compute a coordinate system where epipolar lines are globaly horizontal. This requirement is a consequence of Equation (4), and is illustrated in Figure 6:

- The left image of Figure 6 presents a case where epipolar curve are quasi-vertical and for which an epipolar correction of Equation (4), without an initial rotation, is impossible;
- The center image of Figure 6 presents a case where epipolar curve are slanted; In this case epipolar correction according to equation (4) is possible but leads to important distorsion in the image, as can be seen in the image on the right.

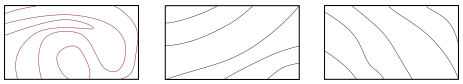

Figure 5. Epipolar lines. Left: not handled by our method; Middle and right: acceptable by our method.

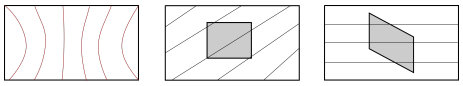

Figure 6. Left: Quasi-vertical epipolar curve for which correction with Equation (4) is impossible. Middle and right: slanted curves for which epipolar rectification with Equation (4) is possible but generates significant distortion.

Therefore, for each image we estimate the average direction $\vec{D}_k$ of their epipolar lines, and a rotation R_k is applied on the input set of points p:

$$R_k(p) = \frac{p - C_k}{\vec{D}_k}, \tag{6}$$

where C_k is the centroid of the set of points. The epipolar lines are now globally horizontal and the subsequent epipolar deformation is computed on the rotated data points.

3.1.4 Layout The layout of the method follows three steps: (1) estimate the global direction of epipolar lines; (2) estimate F_1, F_2 as the local epipolar rectification in the coordinate system linked to the global direction; (3) estimate the final epipolar rectification as a composition of F_1, F_2 and the rotation. A more formalized description of the algorithm is given in Algorithm 1.

Algorithm 1 Epipolar(π_1,π_2). *Layout of the algorithm for computing the epipolar rectification from camera models*

Use π_1, π_2 to estimate a set of *H-Compatible* points $\mathcal{H} = \{(p_1, p_2)\}$:
Estimate centers C_1 and C_2;
Estimate global direction of epipolars $\vec{D}_1$ and $\vec{D}_2$,
Estimate rotations R_1, R_2 according to Equation (6)
for all $p_1, p_2 \in \mathcal{H}$ **do**
  set: $q_1 = R_1(p_1)$, $q_2 = R_2(p_2)$
  add equation: $V_1(q_1) = V_2(q_2)$
end for
estimate with the least squares method V_1 and V_2
set $F_k(x, y) = (x, V_k(x, y))$
set $\phi_k = F_k \circ R_k$
return (ϕ_1, ϕ_2)

3.1.5 Why does our method work? Intuitively, it may not be obvious that the system of equations in Equation (5) is well posed. In fact, if there was a functional relationship between p_1 and p_2, as $p_1 = F(p_2)$, an infinity of solutions for (V_1, V_2) would exist, because for any function $V : \mathbb{R}^2 \to \mathbb{R}$ we can generate a solution $(V, V \circ F)$. However, note that due to the 3D aspect of p_1 and p_2, there is *no* functional relationship between them which leads to a more constrained system of equations. Instead of a functional relationship, we can generate ”one to many” (and ”many to one”) correspondences as illustrated in Figure 7. For example, for a given point p_1, following the curve $\pi_2(\mathcal{B}_1(p_1))$, we can generate several points on the bundle (potentially an infinity) which results in many correspondences. To

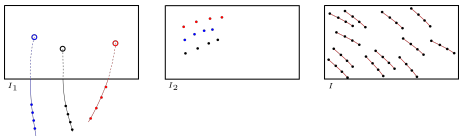

Figure 7. Left: For each p_1, we generate several 3D points on $B_1(p_1)$. Middle: The multiple correspondences in I_2. Right: A dense network of curves in I_2.

illustrate, if we take p_2^k to be k homologous points of p_1, we then have the equation:

$$V_1(p_1) = V_2(p_2^1)\ ;\ V_1(p_1) = V_2(p_2^2)\ ;\ V_1(p_1) = V_2(p_2^3)\ldots, \tag{7}$$

which in fact enforces this constraint:

$$V_2(p_2^1) = V_2(p_2^2) = V_2(p_2^3)\ldots \tag{8}$$

If we now look at left image of Figure 7, we see that Equation (8) imposes the constraint that a ”piece of curve” is horizontal. In Section 3.3.1, we will see a more detailed analysis explaining how the method can work even with configurations different than those depicted in Figure 7.

3.2 Detailed implementation

3.2.1 Choice of a parametric functional space We need to select a space of parametric functions to represent V_1, V_2. The only constraint is that V_1, V_2 are $\mathcal{C}^\infty$ functions, and that the additional constraint in Equation (3) is valid.

Classically, when parameterizing a set of functions $\mathcal{C}^\infty$, a ”natural” candidate is the set of polynomials of a given degree. We know that the function will be $\mathcal{C}^\infty$ and, according to the theorem (Weierstrass, 1885, Stone, 1937) theorem (which says that the space of polynomials is dense in the space of continuous functions), with a sufficiently high degree we will be able to accurately approximate any continuous function. A possible limitation of selecting high degree polynomial is over-fitting, which may lead to unwanted high frequency behavior. In our case, this problem should never arise as the measurements are synthesized from the projection functions π_1, π_2, which provides sufficient redundancy (for instance, hundreds of times more measurements than constraints). Note, however, that some precautions must be taken with respect to the polynomial degree when using our method with image correspondences, without the geometric model (see Section 3.3.1). If d is the selected degree, the two vectors of unknowns $C_{a,b}^1, C_{a,b}^2$, corresponding to coefficients of the polynomials are:

$$V_k(p) = V_k(i,j) = \sum_{a=0}^{d}\sum_{b=0}^{d-a} C_{a,b}^k i^a j^b. \tag{9}$$

3.2.2 Imposing constraints on global lines deformation When applying the constraint of equation (3) to equation (9), we have $i = 0$, hence we can suppress all terms i^a for $a \neq 0$. The constraint equation then reads:

$$V_1(0,j) = j = \sum_{b=0}^{N} C_{0,b}^1 j^b \tag{10}$$

In the equation above, j on the left and the sum on the right are both polynomials. If the two polynoms are equal on a interval, their coefficient must be equal . This constraint fixes the $C_{0,k}^1$: $C_{0,1}^1 = 1$ and $C_{0,k}^1 = 0$ otherwise. Using the Kronecker delta, we can write:

$$C_{0,k}^1 = \delta_{1,k} \tag{11}$$

3.2.3 Generation of points, computation of the direction and centers The points from π_1 and π_2 are generated twice, using each image as the master. The bundles are always generated from the master images. The Algorithm 2 presents the generation of the points with I_1 as the master, as well as the computation of the global direction and the points' centers.

Algorithm 2 GenerateData(). *Compute a list $L_{1,2}$ of $\pi_1 - \pi_2$ H-compatible pairs with I_1 as the master image. Compute also the center C_1 of points in I_1 and the global direction $\vec{D}_2$ for epipolar curves of I_2.*

$L_{1,2} \leftarrow ()$; $C_1 \leftarrow (0,0)$; $\vec{D}_2 \leftarrow \overrightarrow{(0,0)}$; $N \leftarrow 0$
for $p_1.x = 0$ **to** X_1 **Step** $\delta_{x,y}$ **do**
  for $p_1.y = 0$ **to** Y_1 **Step** $\delta_{x,y}$ **do**
    for $z = Z_0$ **to** Z_1 **Step** δ_z **do**
      $p_2 = \pi_2(\widetilde{\pi}_1^{-1}(p_1, Z))$
      $p_2' = \pi_2(\widetilde{\pi}_1^{-1}(p_1, Z + \delta_z))$
      if $p_2 \in I_2$ **and** $p_2' \in I_2$ **then**
        $L_{1,2}.append((p_1, p_2))$
        $C_1 \leftarrow C_1 + p_1$
        $\vec{D}_2 \leftarrow \vec{D}_2 + \frac{\overrightarrow{p_2 p_2'}}{|p_2 p_2'|}$
        $N \leftarrow N + 1$
      end if
    end for
  end for
end for$C_1 \leftarrow \frac{C_1}{N}$; $\vec{D}_2 \leftarrow \frac{\vec{D}_2}{N}$

Once the centers C_1, C_2, directions $\vec{D}_1, \vec{D}_2$ and the list $L_{1,2}$ are computed, they are used to normalize the measurements and make the direction globally horizontal by applying Equation (6) to all elements of the list.

3.2.4 Estimating the rectification As the measurements are synthetic and without outliers, we can directly solve the equations with the linear least squares method. Let's sum up all previous steps. Let d be the degree of the polynomials, and the unknowns are the coefficient of the polynomials V_1 and V_2. There are $\frac{(d+1)(d+2)}{2}$ unknowns for V_2 and $\frac{(d+1)(d+2)}{2} - (d+1)$ for V_1, taking into account the constraint in Equation (11). For each pair of normalized points q_1, q_2 (see Algorithm 1) we add the Equation (9) to the least squares equation system. We then estimate the V_1, V_2 and obtain:

$$\varphi_k(p) = \varphi_k(i,j) = (i, V_k(i,j))\ ;\ \phi_k = \varphi_k \circ R_k \tag{12}$$

Estimating the inverse function The natural way to resample I_k in E_k (see Figure 2) is to write:

$$E_k(p) = I_k(\phi_k^{-1}(p)). \tag{13}$$

Therefore, to rectify an image, we also need to calculate the inverse function. The inverse of R_k is obvious. For computing the inverse of φ_k, we exploit the fact that if φ is invariant for the column, then φ^{-1} is invariant too. Consequently, we can parametrize it with a function $W : \mathbb{R}^2 \to \mathbb{R}$ as:

$$\varphi_k^{-1}(p) = \varphi_k^{-1}(u,v) = (u, W_k(u,v)) \tag{14}$$

To estimate W, we follow the same rationale as in Section 3.2.1, and use the base of a polynomial function. Once the V_k are known, we generate for each point $p_k = (i, j)$ in $L_{1,2}$ an observation:

$$W_k(i, V_k(i, j)) = j \tag{15}$$

If we want to ensure that the computed inverse is sufficiently close to the ”real” inverse, we can increase the polynomial's degree (in our implementation, we typically use the degree of $d + 4$). It has no side effects as long as we maintain high redundancy.

3.3 Epipolar resampling without the geometric model

3.3.1 Resampling with image correspondences only *”Is it possible to use the proposed method to compute the epipolar geometry if we have image point correspondences (i.e., image features) between the image pairs but we don't know their geometric models?”* There is NO straightforward answer to whether it is possible or not. In general, it is not possible, but it becomes possible when the relief (i.e., 3D scene) is not smooth and we constraint the resampling be more or less smooth.
The rationale behind trying to use exclusively image correspondences comes directly from Algorithm 1. As one can see, it does not matter if the point correspondences are extracted with the help of some geometric model (as with Algorithm 2) or from an image processing method not requiring any *a priori* information on image geometry, e.g. SIFT (Lowe, 2004). Hence, as long as we know the directions of the epipolar lines, our method is applicable.
However, when the point correspondences are computed with an image processing routine, there exists some functional relationship between them. Suppose that the 3D scene can be described by a function $Z = \mathcal{Z}(X, Y)$, and denote $S^{\mathcal{Z}}$ as the corresponding surface. For a point p_1 of I_1, denote $\widetilde{\pi}_1^{\mathcal{Z}}(p_1)$ as the intersection of $\mathcal{B}_1(p_1)$ and the surface $S^{\mathcal{Z}}$. Here, the function $\widetilde{\pi}_1^{\mathcal{Z}}$ is the inverse of the projection π_1 which relates the image I_1 and the surface $S^{\mathcal{Z}}$. We now see that there exists a functional relationship between all the point correspondences (p_1, p_2) and it follows this equation:

$$p_2 = (\pi_2 \circ \widetilde{\pi}_1^{\mathcal{Z}})(p_1) = F^{\mathcal{Z}}(p_1). \tag{16}$$

Therefore, as discussed in Section 3.1.5, in the most general case, it is impossible to recover the epipolar geometry from a set of correspondences.
This said, until now we have ignored what we said in Section 3.1.5, namely, that in the proposed method the functions V_1 and V_2 have to be ”smooth”. Let's reason again and suppose we have computed an epipolar geometry: $e_k = (u_k, v_k) = \phi_k(p_k) = (x_k, V_k(y_k)$ with $v_1 = v_2$ and V_k being a ”smooth” function. We now want to analyse whether the geometry was ambiguous. We have

$$e_2 = (\phi_2 \circ \pi_2 \circ \widetilde{\pi}_1^{\mathcal{Z}} \circ \phi_1^{-1})(e_1) = P(e_1),$$

and so, we can write

$$(u_2, v_2) = P(u_1, v_1) = (u_1 + p_x(u_1, v_1), v_1),$$

where p_x is what is usually called the ”parallax function”. As in Section 3.1.5, for any function $W_2 : \mathbb{R}^2 \to \mathbb{R}$, let W_1 be the function defined by $W_1 = W_2 \circ P$. Then, for any (e_1, e_2), $(u_1, W_1(u_1, v_1))$ and $(u_2, W_2(u_2, v_2))$, we also satisfy the epipolar constraint as

$$W_1(u_1, v_1)) = W_2(P(u_1, v_1)) = W_2(u_2, v_2).$$

Is it possible that W_2 and $W_2 \circ P$ are both smooth functions? This depends on the smoothness of P. If P is itself a smooth function, then obviously for any smooth W_2, $W_2 \circ P$ will also be smooth and the epipolar resampling will be ambiguous. If we take the canonical example of a flat 3D scene, then $p_x = 0$, $P = Id$ and as $W_1 = W_2$, W_1 is smooth if W_2 is smooth. In this case the epipolar geometry is also ambiguous. However, if the scene has high frequency depth changes, then P also has high frequencies, and W_2 and $W_2 \circ P$ cannot both be smooth. This can be seen more formally by the following equation:

$$\frac{\partial W_2 \circ P}{\partial u} = \frac{\partial P}{\partial u} \frac{\partial W_2}{\partial u} \circ P. \tag{17}$$

As an example, for any point where the scene is not differentiable, we have $\frac{\partial P}{\partial u} = \infty$, and from the equation above, the term $\frac{\partial W_2}{\partial u} = 0$, because $W_2 \circ P$ is said to be smooth. With a polynomial W_2 of a limited degree and with a sufficient number of points, the term $\frac{\partial W_2}{\partial u} = 0$ leads to the realisation that W_2 depends only on v. Finally, including Equation (3), we have the polynomial $W_2 = Id$, showing the uniqueness of the solution.

3.3.2 Estimating the directions without model To use the resampling method with image features, we need a way to estimate the global directions of the epipolar lines, as it is done in Section 3.1.3 with the help of the geometric model. In the provided implementation we allow the user to provide the directions, or else the directions are computed automatically. For instance, in satellite along-track acquisitions, the user can easily deduce the directions, and it is certainly the ”safer” option. The automated option is based in discretizing a number of directions in each image of a stereo pair, followed by a combinatorial exploration of all possible pairs of directions. For each direction pair, epipolar models (c.f., Section 3.2) with polynomials of degree 0 are computed. The residuals (i.e., the y-parallax) calculated on all image features serve as quality criterion in choosing the final global directions. Since the image features may contain outliers, residuals are evaluated using $L1$ norm.
Once the directions are known, the resampling polynomial is robustly calculated with a weighted iterative least-square approach as follows:

1. Start with 1^{st} degree polynomial and evaluate it with $L1$ norms;
2. Then, use the previous solution to weight the observations and evaluate 3^{rd} degree polynomial with the weighted least-squares method;
3. Then, use the previous solution to weight the observations and evaluate 5^{th} degree polynomial with the weighted least-square method; etc.

4. Numerical experiments

We demonstrate the performance of the algorithm in two scenarios: with and without the geometric model of the camera. The results are evaluated in terms of the remaining *y-parallaxes*, and compared to competetitors: the method by (Oh, 2011) for pushbroom geometries, and a resampling method implemented in MicMac for calibrated central perspective geometries (we refer to it as the *classical* method). The latter is equivalent of the

epipolar resampling proposed by (Fusiello et al., 2000) with the exception that it handles camera distortion parameters, hence, it does not require the undistorting of the images prior to the rectification. We evaluate our method against the central perspective geometry only for comparison purposes, because we dispose of ground truth epipolar geometries for this camera model. In practice, the classical method, which is founded on physical modeling with a minimal number of unknown, should be preferred.

To generate points correspondences in Algorithm 2, when the camera geometry is known, the points in the image space are defined as a grid of 100×100. The Z is the mean depth of the scene, and the step δ_Z is set such that 3 evenly distributed depths spaning the 3D space are obtained. Additionally, each image point is assigned a 4^{th}, random depth for evaluation. The min/max depths representing the envelope of the 3D scene, can be inferred from the RPCs or from depths of the sparse structure (see Z_{buff} in Table 1).

Influence of different geometries of acquisition. Five Pléiade-1A images with their corresponding RPC geolocations are first refined in a RPC-bundle adjustment (Rupnik et al., 2016). We then form pairs of images of varying base-to-height ratios ($^B/_H$) in the range $\in \langle 0.1, 0.45 \rangle$, and carry out epipolar resampling with *Ours* and Oh's methods. We also distinguish between *single orbit* and *multiple orbit* configurations. In Table 1 the maximum values of the remaining y-parallax are reported. The y-parallax is computed on a grid of image points generated with Algorithm 2. Note that these points are non-overlapping with the grid used for estimating the resampling polynomials. We can see that *Our* method outperforms the method by Oh in all instances and is insensitive to the acquisition geometry.

Comparison of resampling with and without the camera geometry. To evaluate the performance of the proposed method on images without known camera geometry, we run epipolar resampling twice: with the camera model, and using SIFT features (Lowe, 2004). In the latter scenario, the resampling polynomial was found across 6 iterations by progressively increasing the degree (the final polynomial being of 6^{th} degree). The comparison is done on a pair of Pléiade-1A images. In Figure 8 the per-pixel y-parallaxes are given. In all three scenarios the remaining parallax is of the same magnitude, $error_y < |0.05|$ pixel. The *Oh* and *Ours* method with the camera model give comparable results, while the approach with SIFT correspondences is clearly the best. The experiments with the camera model reveal a correlation between the remaining y-parallax and the 3D scene geometry. We believe this is due to unmodelled errors in RPC camera model. The approach based on SIFT correspondences uses points and is independent of the camera model hence no systematic error is present in the y-parallax map.

Epipolar resampling of panoramic pushbroom camera Corona KH-4B images are analog images captured by the american reconnaissance satellites in the Cold War period (Madden, 1996). Since 1995 many Corona images are declassified and available to the public. Image processing and photogrammetry with Corona images remains difficult because the camera geometry is complex (Sohn et al., 2004, Ghuffar et al., 2022), and camera calibration certificates are rarely provided. In the absence of the known camera parameters, epipolar rectification with image features is an interesting alternative to allow for

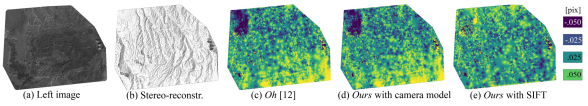

Figure 8. Comparison of epipolar resampling with and without the camera geometry. (c)-(d) correspond to the per-pixel y-parallax computed with dense image matching in the direction perpendicular to the epipolar line.

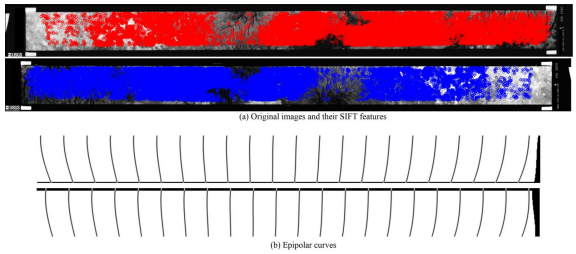

Figure 9. Corona KH-4B stereo pair.

stereo-reconstruction. Figure 9 shows the image pair in its native geometry (i.e., panoramic pushbroom), the SIFT features extracted on the full resolution images, as well as the epipolar curves. The resampling polynomial was found across 9 iterations by progressively increasing its degree (the final polynomial being of 9^{th} degree). As no ground truth is available, we evaluate the dataset visually in Figure 10 by providing a semi-global matching stereo-reconstruction and by drawing some epipolar lines. Because the images are subject to various distortions (i.e., panoramic, image scanning or image motion compensation distortions) as explained in (Gheyle et al., 2011), the remaining y-parallax in Figure 8(c) manifests systematic errors up to $|0.5|$ pix. Such errors cannot be modelled with the chosen polynomial functions.

Epipolar resampling of central perspective camera The experiments with the central perspective camera have a double objective. First we show that the proposed method works with pinhole cameras, and second we demonstrate the ambiguity of epipolar resampling when the scene can be represented by a smooth function, e.g., when it is flat (see Section 3.3.1). In Figure 11 the experiments are referred to as *Stairs* and *Floor*. The *Stairs* is an image pair of a staircase, so it is not flat. The *Floor*, as the name suggests, corresponds to the image pair of a floor, which is globally planar. We can observe that the epipolar resamplings computed with the camera models are comparable to the epipolar resampling with the *classical* method.
The experiment with the SIFT features is a confirmation of the theoretical analysis developped in Section 3.3 : with tie point only, it is possible to recover the epipolar geometry *if and only if* the relief contains high frequencies. Here method based on the SIFT features works well when the scene has a relief, and as expected fails on the planar scene (see the deformed epipolar image pair and the respective epipolar curves in Figure 11(c),(f)).

5. Conclusions

We have presented of rigorous mathematical analysis of the epipolar resampling problem. In particular, we established the necessary and sufficient condition for the existence of an exact epipolar resampling and, when this condition is satisfied, established the degree of ambiguity of epipolar resampling. From this analysis we have derived a method for epipolar resampling

This contribution has been peer-reviewed. The double-blind peer-review was conducted on the basis of the full paper.
https://doi.org/10.5194/isprs-annals-XI-2-2026-17-2026

(a) Acquisitions from a single orbit.

	(Oh, 2011)				Ours			
	B/H				B/H			
Z_{buff} [m]	0.1	0.15	0.25	0.45	0.1	0.15	0.25	0.45
270	0.0055	0.0156	0.0144	0.0010	0.0036	0.0026	0.0026	0.0020

(b) Acquisitions from multiple orbits.

Z_{buff} [m]	0.13	0.2	0.3	0.4	0.13	0.2	0.3	0.4
270	0.0381	0.0311	0.0343	0.0340	0.0101	0.0171	0.0143	0.0154

Table 1. Maximum value of the remaining y-parallax [pix]. Z_{buff} corresponds to half the depth of the volumne used in the resampling calculation. Residual color-coding: min max

of a generic pair of sensors that works as long a the existence criteria is approximately satisfied. The method computes the resampling functions by fitting analytical models which induce no deformation along the x-axis, and minimizes the y-parallax . We have demonstrated that the approach performs well on various camera geometries (central perspective, pushbroom, pushbroom panoramic). Experiments also showed suitability of the approach to resampling images with only image correspondences, when camera geometry is unknown. Note that the proposed method is not suitable for resampling images with large variations in the epipolar line directions. Future works include applying the method to multi-modal images, e.g. optical and radar.

References

Darmon, F., Monasse, P., 2021. The Polar Epipolar Rectification. *Image Processing On Line*, 11, 56–75. `https://doi.org/10.5201/ipol.2021.328`.

de Franchis, C., Meinhardt-Llopis, E., Michel, J., Morel, J.-M., Facciolo, G., 2014. On stereo-rectification of pushbroom images. *2014 IEEE International Conference on Image Processing (ICIP)*, IEEE, 5447–5451.

Fusiello, A., Irsara, L., 2008. Quasi-euclidean uncalibrated epipolar rectification. *2008 19th International Conference on Pattern Recognition*, IEEE, 1–4.

Fusiello, A., Trucco, E., Verri, A., 2000. A compact algorithm for rectification of stereo pairs. *Machine vision and applications*, 12(1), 16–22.

Gheyle, W., Bourgeois, J., Goossens, R., Jacobsen, K., 2011. Scan problems in digital CORONA satellite images from USGS Archives. *Photogrammetric Engineering & Remote Sensing*, 77(12), 1257–1264.

Ghuffar, S., Bolch, T., Rupnik, E., Bhattacharya, A., 2022. A Pipeline for Automated Processing of Declassified Corona KH-4 (1962–1972) Stereo Imagery. *IEEE Transactions on Geoscience and Remote Sensing*, 60, 1-14.

Gupta, R., Hartley, R. I., 1997. Linear pushbroom cameras. *IEEE Transactions on pattern analysis and machine intelligence*, 19(9), 963–975.

Hartley, R. I., 1999. Theory and practice of projective rectification. *International Journal of Computer Vision*, 35(2), 115–127.

Isgrò, F., Trucco, E., 1999. On robust rectification for uncalibrated images. *Proceedings 10th International Conference on Image Analysis and Processing*, IEEE, 297–302.

Liao, P., Chen, G., Zhang, X., Zhu, K., Gong, Y., Wang, T., Li, X., Yang, H., 2022. A linear pushbroom satellite image epipolar resampling method for digital surface model generation. *ISPRS Journal of Photogrammetry and Remote Sensing*, 190, 56-68.

Lipson, L., Teed, Z., Deng, J., 2021. Raft-stereo: Multilevel recurrent field transforms for stereo matching. *2021 International conference on 3D vision (3DV)*, IEEE, 218–227.

Loop, C., Zhang, Z., 1999. Computing rectifying homographies for stereo vision. *Proceedings. 1999 IEEE Computer Society Conference on Computer Vision and Pattern Recognition (Cat. No PR00149)*, 1, IEEE, 125–131.

Lowe, D. G., 2004. Distinctive image features from scale-invariant keypoints. *International Journal of Computer Vision*, 60(2), 91–110.

Madden, F., 1996. The CORONA camera system: Itek’s contribution to world stability, self-published.

Morgan, M., Kim, K.-O., Jeong, S., Habib, A., 2006. Epipolar resampling of space-borne linear array scanner scenes using parallel projection. *Photogrammetric Engineering & Remote Sensing*, 72(11), 1255–1263.

Oh, J., 2011. Novel Approach to Epipolar Resampling of HRSI and Satellite Stereo Imagery-based Georeferencing of Aerial Images. PhD thesis, The Ohio State University.

Okamoto., A., Ono, T., Akamatsu, S., Fraser, C., Hattori, S., H., H., 1999. Geometric Characteristics of Alternative Triangulaion Models for Satellite Imagery. *Proceedings of ASPRS 1999 Annual Conference*.

Ono, T., 1999. Epipolar resampling of high resolution satellite imagery. *Joint Workshop of ISPRS WG I/1, I/3 and IV/4 Sensors and Mapping from Space*, Citeseer.

Pascal Monasse, Jean-Michel Morel, Z. T., 2010. Three-step image rectification. *BMVC*, 89, 1-10.

Rupnik, E., Pierrot-Deseilligny, M., Delorme, A., Klinger, Y., 2016. Refined Satellite Image Orientation in the Free Open-Source Photogrammetric Tools Apero/MicMac. *ISPRS Ann. Photogramm. Remote Sens. Spatial Inf. Sci.*

Sohn, H.-G., Kim, G.-H., Yom, J.-H., 2004. Mathematical modelling of historical reconnaissance CORONA KH-4B imagery. *The Photogrammetric Record*, 19(105), 51–66.

Stone, M. H., 1937. Applications of the theory of Boolean rings to general topology. *Transactions of the American Mathematical Society*, 41(3), 375–481.

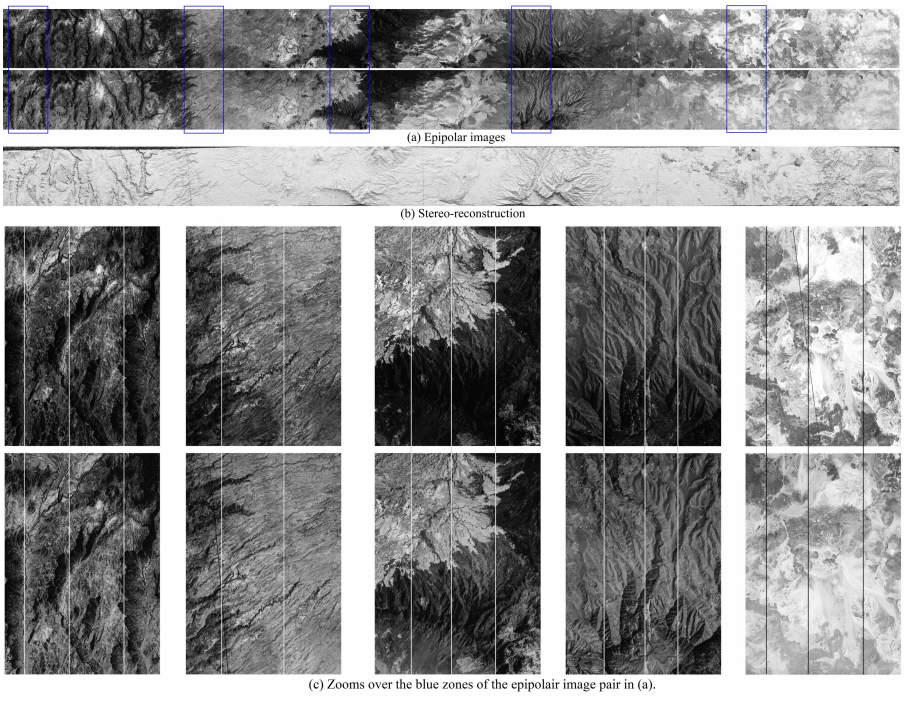

Figure 10. Epipolar images generated from a Corona KH-4B stereo pair, its stereo-reconstruction and the remaining y-parallax. Epipolar lines are marked in white.

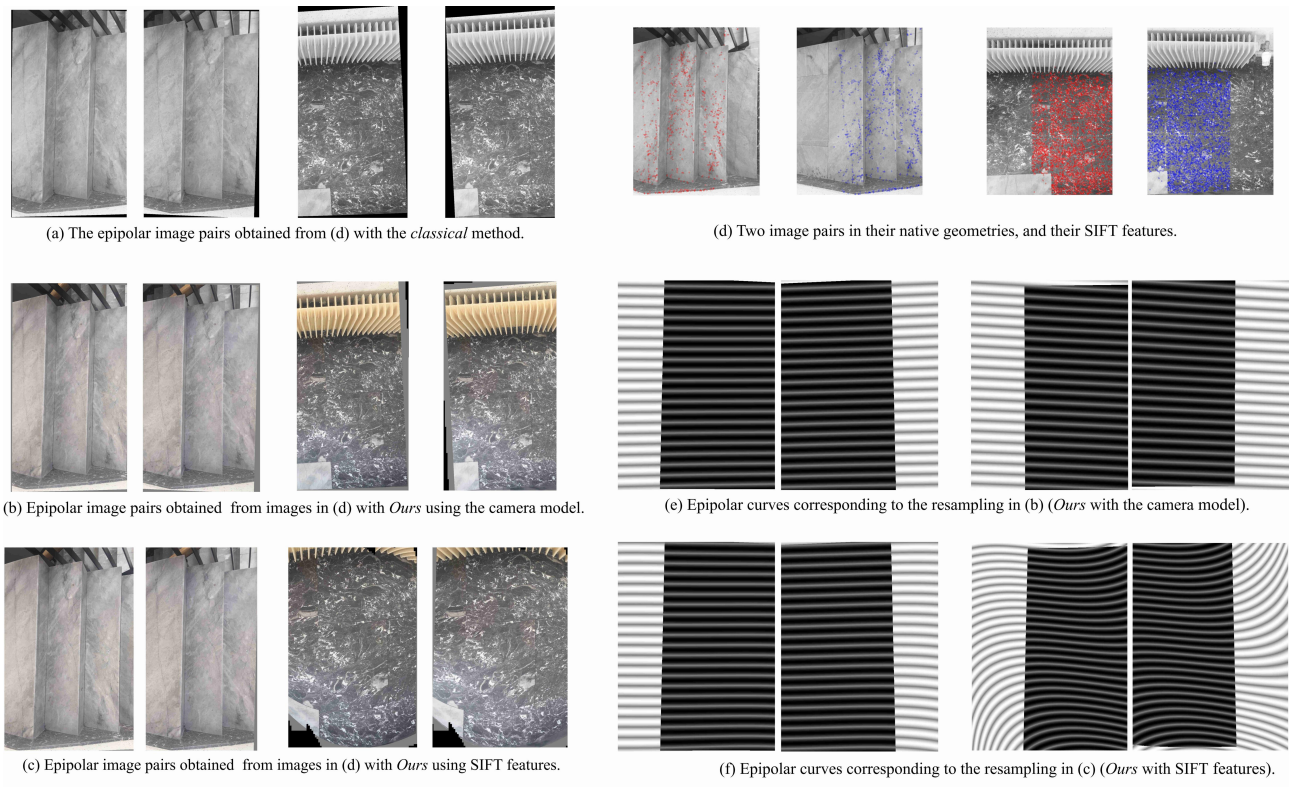

Figure 11. Two experiments (*Staircase* and *Floor*) with the consumer grade camera.

This contribution has been peer-reviewed. The double-blind peer-review was conducted on the basis of the full paper.
https://doi.org/10.5194/isprs-annals-XI-2-2026-17-2026

Wang, J., Chen, M., Karaev, N., Vedaldi, A., Rupprecht, C., Novotny, D., 2025. Vggt: Visual geometry grounded transformer. *Proceedings of the Computer Vision and Pattern Recognition Conference*, 5294–5306.

Wang, M., Hu, F., Li, J., 2011. Epipolar resampling of linear pushbroom satellite imagery by a new epipolarity model. *ISPRS Journal of Photogrammetry and Remote Sensing*, 66(3), 347–355.

Wang, S., Leroy, V., Cabon, Y., Chidlovskii, B., Revaud, J., 2024. Dust3r: Geometric 3d vision made easy. *Proceedings of the IEEE/CVF conference on computer vision and pattern recognition*, 20697–20709.

Weierstrass, K., 1885. Über die analytische Darstellbarkeit sogenannter willkürlicher Functionen einer reellen Veränderlichen. *Sitzungsberichte der Königlich Preußischen Akademie der Wissenschaften zu Berlin*, 2, 633–639.

Wu, H.-H. P., Yu, Y.-H., 2005. Projective rectification with reduced geometric distortion for stereo vision and stereoscopic video. *Journal of Intelligent and Robotic Systems*, 42(1), 71–94.

Xu, G., Wang, X., Ding, X., Yang, X., 2023. Iterative geometry encoding volume for stereo matching. *Proceedings of the IEEE/CVF conference on computer vision and pattern recognition*, 21919–21928.

A. Appendix : The maths of epipolar geometry in the generic case

A.1 Formalisation and notation of projections

We define the geometric sensor model of an image by a projection function π, that computes, for a given 3D point, its 2D projection in the image:

Definition 1 (Generic sensor model)**.** *A geometric sensor model π is a $\mathcal{C}^\infty$ mapping from ground space $(\mathbb{R}^3)$ to image space $(\mathbb{R}^2)$:*

$$\pi : \mathbb{R}^3 \to \mathbb{R}^2, (X, Y, Z) \to (i, j) = \pi(X, Y, Z). \tag{18}$$

Next, we define the bundles of a projection:

Definition 2 (Bundle)**.** *For $p_k \in I_k$ we note $\mathcal{B}_k(p_k)$ the bundle corresponding to $\pi_k^{-1}(p_k)$. When there is no ambiguity, we note identically $\mathcal{B}_k(P)$, where $P \in \mathbb{R}^3$, the bundle corresponding to $\pi_k^{-1}(\pi_k(P)) = \mathcal{B}_k(\pi_k(P))$.*

Later, for simplicity, we will use the quasi-vertical hypothesis, which allows us to extend π to a bijective mapping of $\mathbb{R}^3$ and compute its inverse.

Definition 3 (Quasi-vertical camera model)**.** *We say that the projection is quasi-vertical if the following mapping $\widetilde{\pi}$ is a diffeomophism of $\mathbb{R}^3$:*

$$\widetilde{\pi} :\ \mathbb{R}^3 \to \mathbb{R}^3, \quad (X, Y, Z) \mapsto (i, j, Z) = \widetilde{\pi}(X, Y, Z), \quad \text{with } (i, j) = \pi(X, Y, Z). \tag{19}$$

Given 2 images I_1 and I_2, the knowledge of their geometric models π_1 and π_2 reduces the matching between 2 images to a 1D problem. In fact, given a point p_1 in I_1, we can compute the 3D curve $\mathcal{B}_1(p_1)$ of ground points that project to p_1 in I_1, and compute its homologous curve in I_2 with $\pi_2(\mathcal{B}_1(p_1))$. We now define the H-compatible relation between two points by the following definition:

Definition 4 (H-Compatible, $\overset{\Longleftrightarrow}{\pi_1,\pi_2}$)**.** *We say that p_1 in I_1 and p_2 in I_2 are $\pi_1 - \pi_2$ H-compatible, and write $p_1 \overset{\Longleftrightarrow}{\pi_1,\pi_2} p_2$, if the following condition is satisfied:*

$$\begin{aligned}(\mathcal{B}_1(p_1) \cap \mathcal{B}_2(p_2) \neq \emptyset) \Leftrightarrow \\ (\exists P \in \mathbb{R}^3 : \pi_1(P) = p_1, \pi_2(P) = p_2).\end{aligned} \tag{20}$$

In image matching, the relationship $p_1 \overset{\Longleftrightarrow}{\pi_1,\pi_2} p_2$ means that p_1 and p_2 are potentially homologous.

A.2 Definition of the epipolar geometry

The relationships described above are sufficient to implement standard matching techniques, and (π_1, π_2) can be used to define a matching process that leverages *a priori* geometric knowledge of the scene. Given a point in one image, its curve of potentially corresponding points in the other image can be readily traced. This approach, which does not rely on epipolar geometry, has the additional advantage of being directly applicable to multi-image matching. Epipolar geometry is therefore not strictly necessary for establishing image correspondences. However, this strategy combines two tasks within a single procedure: handling the geometric transformations and resampling, and performing the actual matching. When only a single image pair is considered, epipolar geometry provides a more elegant solution by decoupling these tasks into two independent problems.

Definition 5 (Epipolar Geometry)**.** *Let π_1, π_2 be two cameras and let ϕ_1, ϕ_2 be two diffeomorphisms of $\mathbb{R}^2$. We say that ϕ_1, ϕ_2 are an epipolar resamplings iff:*

$$\begin{aligned}\forall e_1 = (u_1, v_1), e_2 = (u_2, v_2) : (v_1 = v_2) \Leftrightarrow \\ (\phi_1^{-1}(e_1) \overset{\Longleftrightarrow}{\pi_1,\pi_2} \phi_2^{-1}(e_2)).\end{aligned} \tag{21}$$

The matching of epipolar images is simplified because we know that the lines in two images are globally homologous.

Notation 1 (Epipolar line and curve)**.** *We denote $\mathcal{L}_k(v)$ as the epipolar line of E_k defined by $v_k = v$. We also denote $\mathcal{C}_k(v)$ as the epipolar curve of I_k defined by $\mathcal{C}_k(v) = \phi_k^{-1}(\mathcal{L}_k(v))$*

We can see that when epipolar geometry exists, the two curves $\mathcal{C}_1(v)$ and $\mathcal{C}_2(v)$ are globally homologous:

$$\mathcal{C}_1(v) = \pi_1(\pi_2^{-1}(C_2(v))); \mathcal{C}_2(v) = \pi_2(\pi_1^{-1}(C_1(v))). \tag{22}$$

A.3 Existence of the epipolar geometry

As we will show, an epipolar geometry generally does not exist for many imaging configurations, and when it does, it may not be unique. For any image pair acquired under a central projection, an epipolar geometry is guaranteed to exist. In contrast, for projection models such as the cylindrical projection characteristic of many pushbroom satellites, a rigorous epipolar resampling cannot be defined (although close approximations can

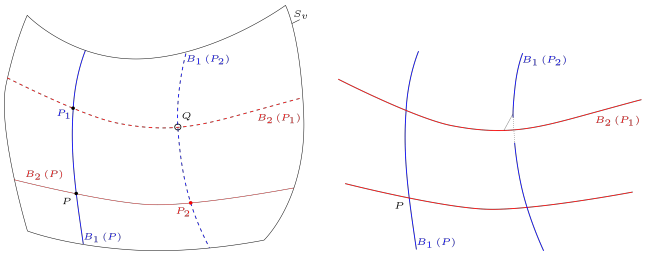

Figure 12. Path closure. Left: in the epipolar case, the bundles are on the same level of the foliation and the intersection. Right: in the generic case, the paths don’t intersect and no epipolar geometry exists.

often be constructed in practice). We explain now why the epipolar geometry does not exist for any projections π_1, π_2 and is instead an exception. Let’s define the surface $\mathcal{S}_v^k$ of $\mathbb{R}^3$ by:

$$\mathcal{S}_v^k = \pi_k^{-1}(\mathcal{C}_k(v)). \tag{23}$$

Following the definition of epipolar geometry above, it can be seen that $\mathcal{S}_v^1$ and $\mathcal{S}_v^2$ are the same surface $\mathcal{S}_v$:

$$\mathcal{S}_v^1 = \mathcal{S}_v^2 = \mathcal{S}_v. \tag{24}$$

In fact, for any $P \in \mathcal{S}_v^1$, set $e_1 = \phi_1(\pi_1(P)) = (u_1, v)$ and $e_2 = \phi_2(\pi_2(P)) = (u_2, v_2)$. We then have $\pi_1(P) \overset{\pi_1, \pi_2}{\longleftrightarrow} \pi_2(P)$ because they are projections of the same point. Then, $v_2 = v$ according to Definition 5, and $P \in \mathcal{S}_v^2$. Furthermore, the $\mathcal{S}_v$ defines a foliation of $\mathbb{R}^3$, and it can be seen that:

$$\forall v \forall P \in \mathcal{S}_v : \mathcal{B}_1(P) \subset \mathcal{S}_v, \mathcal{B}_2 \subset \mathcal{S}_v, \tag{25}$$

which also leads directly from the definitions above because if $P \in \mathcal{S}_v$ then $\pi_k^{-1}(P) \in \mathcal{C}_k(v)$ (see Equation (23)), and $\pi_k^{-1}(\pi_k(P)) = \mathcal{B}_k(P) \subset \mathcal{S}_v$. However, in general, the existence of a stable foliation for the two bundle sets, as expressed in Equation (25), cannot be satisfied. We illustrate it in Figure 12. Furthermore, let π_1 and π_2 be again any two projections and suppose there exists a foliation satisfying the Equation (25). Then, let:

- P be any point in 3D space, and $\mathcal{S}_v$ be the surface such that $P \in \mathcal{S}_v$;
- $P_1 \neq P$ be a point on 3D curve $\mathcal{B}_1(P)$, $P_1 \in \mathcal{S}_v$, then $\mathcal{B}_2(P_1) \subset \mathcal{S}_v$;
- $P_2 \neq P$ be a point on 3D curve $\mathcal{B}_2(P)$, $P_2 \in S_v$, then $\mathcal{B}_1(P_2) \subset \mathcal{S}_v$.

As $\mathcal{B}_2(P_1)$ and $\mathcal{B}_1(P_1)$ are included in the same surface $\mathcal{S}_v$, they must intersect somewhere in a point Q. In the general case, the above statement is a contradiction because there is no reason that the condition $\mathcal{B}_2(P_1) \cap \mathcal{B}_1(P_2) \neq \emptyset$ is satisfied for any two sets of bundles (see Figure 12, right).

A.4 A local characterization of the epipolar existence

In this section, we derive a local formula (i.e. a differential equation) that measures the existence of an epipolar geometry. We refer to it as the *epipolarability index*.

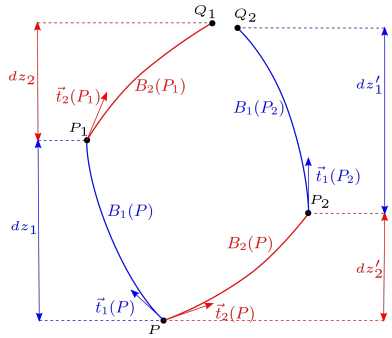

Figure 13. Notation for local characterization of the epipolar existence.

Analogously to the proof in Section A.3, we will make a computation of two-way paths, $\mathcal{B}_1$ then $\mathcal{B}_2$, as well as $\mathcal{B}_2$ then $\mathcal{B}_1$. Then, we express the Taylor expansion of the intersection distance between these two paths. For sake of simplicity, let’s suppose that we are in a quasi-vertical acquisition geometry stated in Definition 3[1], and in Figure 13, and the point P is any point in $\mathbb{R}^3$. We then denote:

- the first path (P, P_1, Q_1) following $\mathcal{B}_1(P)$ then $\mathcal{B}_2(P_1)$, making a progression δ_1 on $\mathcal{B}_1(P)$ and δ_2 on $\mathcal{B}_2(P_1)$;
- a second path (P, P_2, Q_2) following $\mathcal{B}_2(P)$ then $\mathcal{B}_1(P_2)$, making a progression δ'_2 on $\mathcal{B}_2(P)$ and δ'_1 on $\mathcal{B}_1(P_2)$;
- $\overrightarrow{t_1(P)} = (x, y, 1)$ as the tangent to the bundle $\mathcal{B}_1$ in point P (and similarly $\overrightarrow{t_2}(P)$);
- and write $\frac{\partial F}{\partial z_1}$ to refer to the coordinate system $(i_1, j_1, z) = \widetilde{\pi}_1^{-1}(x, y, z)$, idem for $\frac{\partial F}{\partial z_2}$, and obviously as they are two different coordinate systems, we have in general $\frac{\partial F}{\partial z_1} \neq \frac{\partial F}{\partial z_2}$.

Now, for any pair of ”small” values (δ_1, δ_2), we compute (δ'_1, δ'_2) which minimize the distance $|Q_1, Q_2|$ and express the canceling of the second degree Taylor expansion of this distance (the first degree can always be canceled out as we will see). Noting δ the max of all δ, the second degree Taylor expansion gives:

$$\begin{aligned} P_1 = P + \delta_1 \overrightarrow{t_1(P)} + \\ \frac{{\delta_1}^2}{2} \frac{\partial \overrightarrow{t_1}}{\partial z_1}(P) + \mathcal{O}(\delta^3) \end{aligned} \tag{26}$$

$$Q_1 = P_1 + \delta_2 \overrightarrow{t_2(P_1)} + \frac{{\delta_2}^2}{2} \frac{\partial \overrightarrow{t_2}}{\partial z_2}(P_1) + \mathcal{O}(\delta^3) \tag{27}$$

$$\overrightarrow{t_2(P_1)} = \overrightarrow{t_2(P)} + \delta_1 \frac{\partial \overrightarrow{t_2}}{\partial z_1}(P) + \mathcal{O}(\delta^2) \tag{28}$$

Putting together Equations (26), (27), (28) we can perform a Taylor expansion of the path P to Q_1:

$$\begin{aligned} Q_1 = P + \delta_1 \overrightarrow{t_1(P)} + \delta_2 \overrightarrow{t_2(P)} \\ + \frac{{\delta_1}^2}{2} \frac{\partial \overrightarrow{t_1}}{\partial z_1}(P) + \frac{{\delta_2}^2}{2} \frac{\partial \overrightarrow{t_2}}{\partial z_2}(P) + \delta_1 \delta_2 \frac{\partial \overrightarrow{t_2}}{\partial z_1}(P) + \mathcal{O}(\delta^3) \end{aligned} \tag{29}$$

[1] Note that we could use curvilinear abscissa when this assumption is not be satisfied.

And similarly for P to Q_2 :

$$\begin{aligned} Q_2 = P + \delta_2' \overrightarrow{t_2(P)} + \delta_1' \overrightarrow{t_1(P)} \\ + \frac{{\delta_2'}^2}{2} \frac{\partial \overrightarrow{t_2}}{\partial z_2}(P) + \frac{{\delta_1'}^2}{2} \frac{\partial \overrightarrow{t_1}}{\partial z_1}(P) + \delta_1' \delta_2' \frac{\partial \overrightarrow{t_1}}{\partial z_2}(P) + \mathcal{O}(\delta^3) \end{aligned} \tag{30}$$

The first degree Taylor expansion of $Q_2 - Q_1$ gives :

$$Q_2 - Q_1 = (\delta_1' - \delta_1)\overrightarrow{t_1(P)} + (\delta_2' - \delta_2)\overrightarrow{t_2(P)} + \mathcal{O}(\delta^2) \tag{31}$$

To minimize $|Q_2 - Q_1|$, the first step is to cancel the first degree terms of $Q_2 - Q_1$. We assume that $\overrightarrow{t_2(P)}$ and $\overrightarrow{t_1(P)}$ are independant vectors[2] and we must then make $\delta_2' - \delta_2$ and $\delta_1' - \delta_1$ second degree terms:

$$\Delta_1 = \delta_1' - \delta_1 = \mathcal{O}(\delta^2) \; ; \; \Delta_2 = \delta_2' - \delta_2 = \mathcal{O}(\delta^2) \tag{32}$$

To develop $Q_2 - Q_1$ we can use the following identities that are direct consequences of Equation (32):

$$\begin{aligned} \delta_1 \delta_2 - \delta_1' \delta_2' &= \mathcal{O}(\delta^3) \; ; \\ {\delta_1}^2 - {\delta_1'}^2 &= \mathcal{O}(\delta^3) \; ; \\ {\delta_2}^2 - {\delta_2'}^2 &= \mathcal{O}(\delta^3) \; . \end{aligned} \tag{33}$$

Subtracting Equation (29) from Equation (30), and using Equation (33), we can write :

$$\begin{aligned} Q_2 - Q_1 = \Delta_1 \overrightarrow{t_1(P)} + \Delta_2 \overrightarrow{t_2(P)} \\ + \delta_1 \delta_2 \left(\frac{\partial \overrightarrow{t_2}}{\partial z_1}(P) - \frac{\partial \overrightarrow{t_1}}{\partial z_2}(P) \right) + \mathcal{O}(\delta^3) \end{aligned} \tag{34}$$

We now translate the intersection of paths by canceling the second degree Taylor expansion in $Q_2 - Q_1$. We have three vectors, and their weighted sum can be null iff they are colinear.

Theorem 1 (Existence of epipolar geometry)**.** *The epipolar geometry exists iff the following determinant is null:*

$$\left[\begin{array}{c|c|c} \overrightarrow{t_1} & \overrightarrow{t_2} & \frac{\partial \overrightarrow{t_2}}{\partial z_1} - \frac{\partial \overrightarrow{t_1}}{\partial z_2} \end{array} \right] = 0 \tag{35}$$

Remark 1 (Epipolar equation with central perspective camera)**.** *As an illustration on an easy case, we can see that this condition is trivially satisfied for a pair of central perspective cameras as we have the canceling of both terms as shown in Equation* (36)*. This is because for a given point P, and any point P_1 on $\mathcal{B}_1(P)$, $\overrightarrow{t_2(P_1)}$ belongs to the epipolar plane $\mathcal{P}$. We have $\overrightarrow{t_2(P_1)} \in \mathcal{P}$, so $\frac{\partial \overrightarrow{t_2}}{\partial z_1} \in \mathcal{P}$, and as we have also $\overrightarrow{t_1(P)} \in \mathcal{P}, \overrightarrow{t_2(P)} \in \mathcal{P}$, the collinearity between $\overrightarrow{t_1(P)}$, $\overrightarrow{t_2(P)}$ and $\frac{\partial \overrightarrow{t_2}}{\partial z_1}(P)$ is thus proven:*

$$\left[\begin{array}{c|c|c} \overrightarrow{t_1} & \overrightarrow{t_2} & \frac{\partial \overrightarrow{t_2}}{\partial z_1} \end{array} \right] = \left[\begin{array}{c|c|c} \overrightarrow{t_1} & \overrightarrow{t_2} & \frac{\partial \overrightarrow{t_1}}{\partial z_2} \end{array} \right] = 0 \tag{36}$$

A.5 Ambiguity of the epipolar geometry

When the epipolar geometry exists, the epipolar resampling is not unique. To demonstrate that our rectification method handles this ambiguity rigorously, we first describe it formally.

[2] Otherwise, it would be a degenerate case for stereovision

Let ϕ_1, ϕ_2 and ϕ_1', ϕ_2' be two epipolar resamplings. For any v, consider the pair of lines $\mathcal{L}_1(v), \mathcal{L}_2(v)$ for which (see Figure 4 in the main paper):

- $\phi_k^{-1}(\mathcal{L}_k(v))$ is the curve $\mathcal{C}_k(v)$ by definition of epipolar resampling;
- and $\phi_k'(\mathcal{C}_k(v)) = \phi_k'(\phi_k^{-1}(\mathcal{L}_k(v))$ is a line, also by definition of epipolar resampling;
- and in analogy, $\phi_1'(\phi_1^{-1}(\mathcal{L}_1(v))) = \phi_2'(\phi_2^{-1}(\mathcal{L}_2(v)))$.

Consequently we have the following constraints between two pairs of epipolar ressampling:

- $\phi_1' \phi_1^{-1}$ and $\phi_2' \phi_2^{-1}$ are diffeomorphisms transforming lines into lines;
- $\phi_1' \phi_1^{-1}$ and $\phi_2' \phi_2^{-1}$ define the same global transformation on lines (i.e. if $\phi_1'(\phi_1^{-1}(\mathcal{L}_1(v))) = \phi_2'(i\phi_2^{-1}(\mathcal{L}_2(v)))$).

Vice versa, let ϕ_1, ϕ_2 be an epipolar resampling and let Λ_1, Λ_2 be diffeomorphisms that are stable for lines and make globally the same transformation on lines. We can thus note that $\Lambda_1 \circ \phi_1$ and $\Lambda_2 \circ \phi_2$ are also an epipolar resampling (see Figure 4 of the main paper).

Having devised the exact ambiguity, we can now define two constraints to impose on a unique epipolar resampling:

1. **Constraint on the uniqueness of the deformation** inside each line. For instance, one can impose that the colums remain constant (i.e. the deformation is only made on y), as given in Equations (1) and (2);
2. **Constraint on the global deformation** of lines[3]. For instance, by fixing the transformation of one image, as given in Equation (4).

Theorem 2 (Unique epipolar constraint)**.** *If the epipolar geometry exists, there exists a unique epipolar resampling ϕ_1, ϕ_2 satisfying the following three constraints:*

$$\phi_1(x, y) = (x, y') \tag{1}$$

$$\phi_2(x, y) = (x, y') \tag{2}$$

$$\phi_1(0, y) = (0, y) \tag{3}$$

[3] i.e. where each line is transformed globally to another line